MnO Nanocrystals: A Platform for Integration of MRI and Genuine Autophagy Induction for Chemotherapy

14 AUTHORS, INCLUDING:

Li Zhang
Anhui Medical University
30 PUBLICATIONS **172** CITATIONS

SEE PROFILE

Jing Li
Washington University in St. Louis
3 PUBLICATIONS **48** CITATIONS

SEE PROFILE

Yun Liu
Chinese Academy of Sciences
253 PUBLICATIONS **2,247** CITATIONS

SEE PROFILE

Long-Ping Wen
University of Science and Technology of Ch…
80 PUBLICATIONS **4,984** CITATIONS

SEE PROFILE

FULL PAPER

MnO Nanocrystals: A Platform for Integration of MRI and Genuine Autophagy Induction for Chemotherapy

Yang Lu, Li Zhang, Jing Li, Yu-De Su, Yun Liu, Yun-Jun Xu, Liang Dong, Huai-Ling Gao, Jun Lin, Na Man, Peng-Fei Wei, Wei-Ping Xu, Shu-Hong Yu,* and Long-Ping Wen*

Herein, a kind of novel monocomponent hydrophilic and paramagnetic manganese(II) oxide nanocrystal is prepared in polar solution by a one-pot microwave-assisted synthesis. This kind of nanocrystal can be taken up efficiently to serve as an excellent T_1 magnetic resonance imaging (MRI) contrast agent with an enhanced r_1 value of 0.81 mM^{-1} s^{-1}. The key to the success of this method is that no additional capping agents are required for coating onto the surface via ligand exchange, facilitating research of their intrinsic biological activities. Furthermore, multiple lines of convincing evidence are presented to prove that MnO nanocrystals (NCs) elicit p53-activation-independent and authentic functional autophagy via inducing autophagosome formation. Notably, there are very few reports so far of the autophagy phenomenon induced by magnetic nanocrystals. Moreover, these results offer an indication for cancer therapy that MnO NCs combined with doxorubicin at a nontoxic concentration can have a definite synergistic effect, which is mediated through the genuine autophagy induction, on killing cancer cells in vitro and in vivo.

1. Introduction

Exploring outstanding nanomaterials, especially magnetic nanocrystals, to serve simultaneously as both excellent detection probes and cancer therapy agents has been one of the most important tasks in biomaterials.[1–3] Most recent progress has focused on the fabrication of multicomponent nanocomposites to achieve magnetic-resonance (MR)-targeted drug delivery, and magnetic nanomaterials can be facilely combined with mesoporous silica, noble metals, carbon, and fluorescent moieties.[4–8] However, the multicomponents might induce antagonism to perform both MR imaging and chemotherapy at low efficiency in comparison with pure components. Therefore, it is highly desirable to find a monocomponent magnetic nanomaterial that can play a critical role in cancer therapy, while maintaining good properties in MR imaging (MRI).

As MRI agents, magnetic nanocrystals (NCs) can help to enhance the contrast of interesting regions obviously, including tumours and abnormal pathological changes, by decreasing the relaxation time in comparison with that of the surrounding environment.[9] Besides the well-studied T_2-weighted super-paramagnetic MR agents, such as magnetite[10,11] and magnetic alloys,[12–14] paramagnetic materials are mostly utilized for T_1 MRI contrast agents in clinical MRI detection, with commercial gadolinium-diethylene-triamine pentaacetic acid (Gd-DTPA) as an example. Another type of novel biocompatible and paramagnetic nanomaterial for manganese-enhanced MRI (MEMRI) is manganese oxide nanoparticles,[15] which was first reported by Hyeon's group for the selective imaging of breast-cancer cells in mouse brains.[16] Then, the design of ssDNA-immobilizing MnO NCs was reported, for selective activation of the TLR9 pathway in Caki-1 cells.[17] Hollow manganese oxide nanocrystals for MR contrast enhancement and drug loading have also been prepared.[18] Although MnO NCs have demonstrated their excellent T_1 MR imaging capabilities, most recent work on MnO NCs has started with the thermal decomposition of the Mn-oleate complex, which was followed by the transference from organic solution to aqueous solution by surface modification, resulting in a huge limitation for their biological applications.

Autophagy, which is an evolutionarily conserved and highly regulated dynamic intracellular process in mammalian cells for degrading long-lived proteins and the only known pathway for degrading defective organelles, has attracted much attention for the crucial role in physiology and pathology.[19–22] Presently, the constitutively active basal level of autophagy is known

Y. Lu,[+] J. Li, Y.-D. Su, Y. J. Xu, L. Dong, H. L. Gao, Prof. S. H. Yu
Division of Nanomaterials & Chemistry
Hefei National Laboratory for Physical Sciences at the Microscale
Department of Chemistry
CAS Key Laboratory of Mechanical Behavior and Design of Materials
the National Synchrotron Radiation Laboratory
University of Science and Technology of China
Hefei 230026, P. R. China
E-mail: shyu@ustc.edu.cn

L. Zhang,[+] Y. Liu, J. Lin, N. Man, P. F. Wei, Prof. L. P. Wen
Hefei National Laboratory for Physical Sciences
at the Microscale
School of Life Sciences
University of Science and Technology of China
Hefei 230027, P. R. China
E-mail: lpwen@ustc.edu.cn

Dr. Y. J. Xu, Dr. W. P. Xu
Anhui Provincial Hospital
Hefei, 230001, P. R. China

[+] These authors contributed equally to this work.

Materials Views
www.MaterialsViews.com

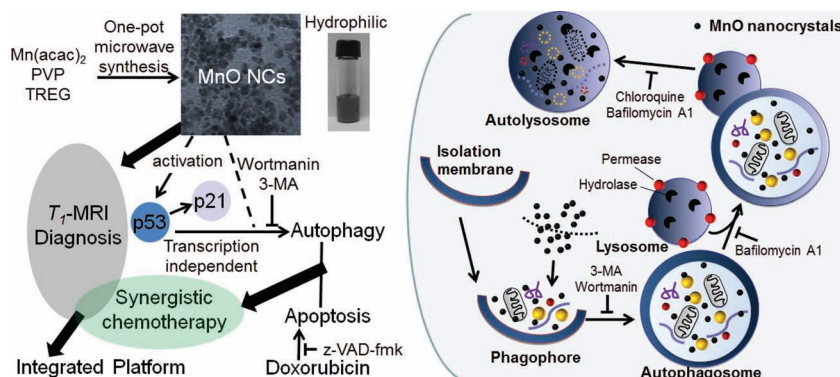ADVANCED
FUNCTIONAL
MATERIALS
www.afm-journal.de

FULL PAPER

to be involved in development, differentiation, homeostasis, and tissue remodeling in various organisms.[23,24] On the other hand, an elevated level of autophagy is frequently observed in cancer cells under a variety of stress situations.[25,26] The effects of elevated autophagy induced by different agents on cell fate, in principle, could have three possibilities: pro-survival, pro-death, or neutral.[27] For instance, some small molecular enhancers of autophagy, such as rapamycin and lithium have shown the protective effect by reducing the toxicity of mutant huntingtin aggregates.[21] However, early-stage studies have described an autophagic cell-death phenomenon manifested by nanosized neodymium oxide; the most-recent investigation revealed extensive infiltration of inflammatory cells in mice treated with lanthanide-based nanocrystals, where the liver toxicity was also associated with nanoparticle-induced autophagy perturbation.[28] In addition, we present that cysteamine, a biocompatible molecule, can enhance the chemotherapeutic effect of doxorubicin via autophagy modulation,[29] indicating that the design of some novel modulators of autophagy, especially nanocrystals, should be of great importance to cancer-cell fate and even chemotherapy enhancement.

Herein, we report that a kind of hydrophilic MnO nanocrystal can be synthesized via a one-pot microwave synthesis in polar solvent, and can serve as an outstanding T_1-MR contrast agent directly. The obtained MnO NCs were found to induce genuine autophagy, and the interaction between MnO NCs and the cellular autophagic signaling pathway have been investigated in detail. The results demonstrate that MnO NCs can provide a useful platform for combinatorial treatment of cancers via the synergistic effects of the nanocrystals and doxorubicin in killing the cancer cells, as illustrated in **Scheme 1**.


Scheme 1. Schematic illustration of the preparation of the MnO nanocrystals for the integration of MRI and genuine autophagy induction for chemotherapy.

2. Results and Discussion

2.1. Preparation of Hydrophilic MnO Nanocrystals

There are five common oxidation states of manganese, and the direct synthesis of hydrophilic manganese(II) oxide nanocrystals is of great challenge. Previously, it was reported that Ni-Co metallic nanorings can be synthesized by solvothermal reduction of nickel (II) and cobalt (II) acetylacetonates in triethylene glycol.[12] Similarly, iron (III) acetylacetonate has been just partly reduced to Fe^{2+} by a polyalcohol, resulting in well-defined ultrafine iron oxide nanocrystals. As neighboring transition metal elements, it is reasonable that manganese (II) pentanedionate could be selected for the synthesis of manganese (II) oxide nanocrystals in polyalcohol without the change of the manganese chemical valence. Herein, we report the synthesis of uniform and high-yield products with a size of 10 nm and water-solubility, via a one-pot microwave-assisted method in a polar solvent, as confirmed by electron microscopy (**Figure 1**a–c). As a polar solvent with a high boiling point and

a strong absorption of microwave irradiation, triethylene glycol (TREG) served as the solvent in the presence of poly(vinyl pyrrolidone) (PVP). Distinct from conventional heating methods, the microwave-assisted synthesis method possesses a good reproducibility for large-scale synthesis, and a holding period of only 10 min is needed. In contrast, the solvothermal products were low-yield, and some large spheres can be observed in Figure 1d, indicating a poor size distribution. All of the X-ray diffraction peaks of the obtained MnO nanocrystals can be indexed as pure face-centered cubic manganosite (MnO), in good agreement with previously reported values (JCPDS no. 89-4835),[30] and no phase transformations were observed in the XRD pattern of their dispersion in phosphate buffered saline (PBS) for one week, indicating the stability of MnO NCs in physiological conditions (Figure 1e). The high-resolution TEM (HR-TEM) image in Figure 1f shows the lattice fringes of the (200) and (111) lattice planes of manganosite MnO, with d spacings of 2.23 and 2.56 Å, respectively. In addition, calculations based on the half-widths of the (200) diffraction peak using the Scherrer formula indicate that the average particle size was about 10 nm, which is similar to MnO NCs prepared by Hyeon's group.[16] The prepared, smaller-sized MnO nanocrystals will contribute more to the T_1 contrast by enhancing the interaction between metal ions and the surrounding water molecules due to their high surface-to-volume ratio compared with large particles. Then, according to the enhanced permeability and retention effect (EPR), the as-prepared PVP-coated, 10 nm, water-soluble manganese oxide nanocrystals should easily pass through the endothelia of newly formed tumor vessels with large fenestrations, and will tend to accumulate in tumor tissue much more than in normal tissues for more-efficient passive targeting.[31]

2.2. Magnetic Behavior and MRI

The hysteresis loop curves of the obtained MnO nanoparticles, shown in **Figure 2**, were found to be different from the anti-ferrimagnetism of MnO in the bulk. The 10 nm MnO nanocrystals displayed paramagnetism at room temperature, while performing ferromagnetism at low temperature, and the observed blocking temperature T_B was 20 K, which was slightly different to the reported value for 10 nm-sized MnO

FULL PAPER
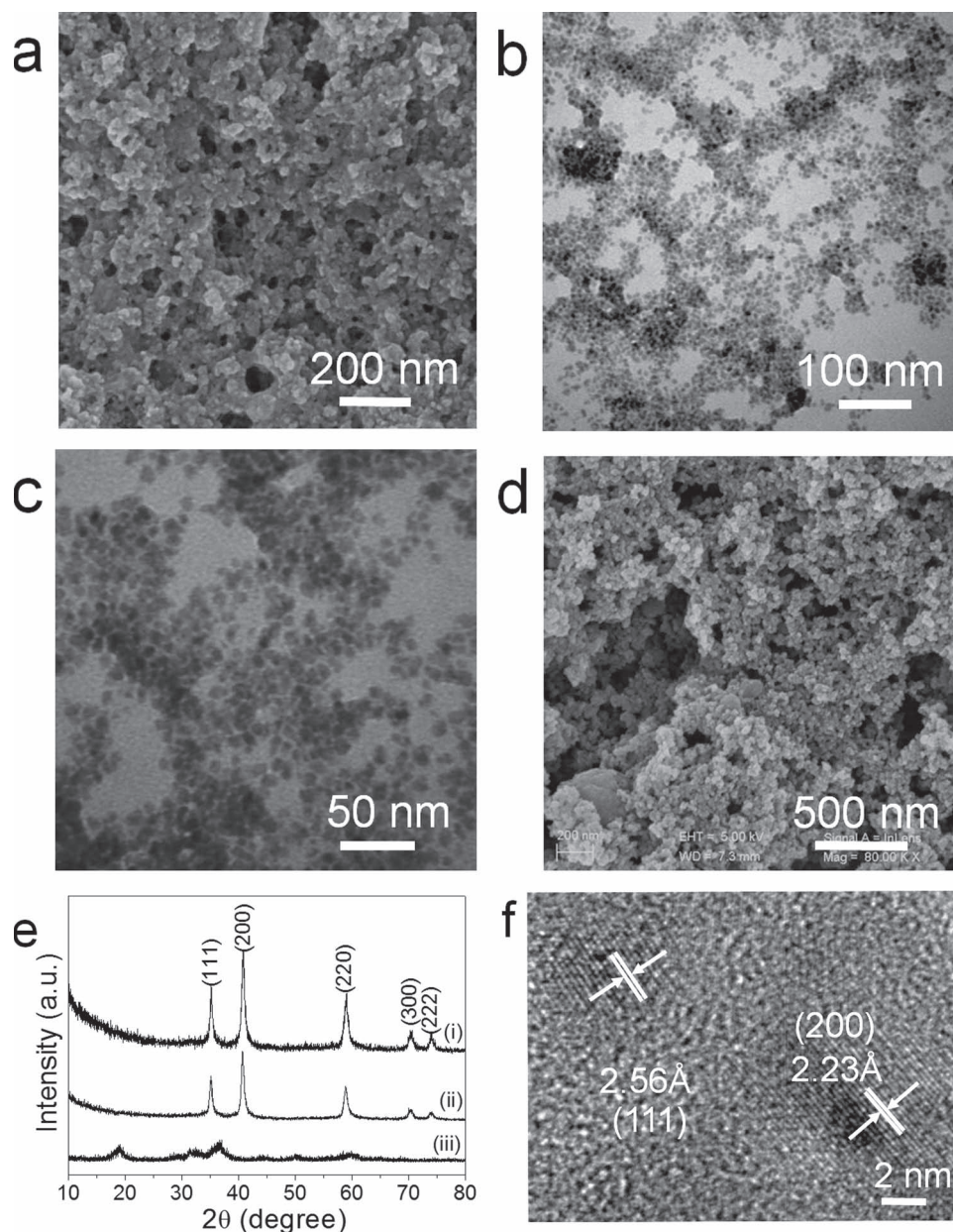
Figure 1. a–c) SEM (a) and TEM images (b,c) of MnO nanocrystals prepared by one-pot microwave-assisted method. d) SEM image of MnO nanocrystals prepared by conventional solvothermal decomposition. e) XRD pattern for microwave-prepared hydrophilic MnO nanocrystals (i), the MnO nanocrystals dispersed in PBS buffer for one week and washed with deionized water several times (ii), and a sample synthesized from Mn(acac)$_3$ (iii). f) HR-TEM image of two typical MnO nanocrystals.

NCs but similar to that of 5 nm-sized MnO NCs.[32] This might be explained in that the magnetic property of the nanomaterials is associated with surface modification, besides their sizes.

The MnO nanocrystals can induce significant T_1-MRI contrast enhancement due to their excellent magnetic properties. As the concentration of as-prepared water-soluble MnO nanocrystals increased from 0.25 to 2 mM, the signals of the samples in the T_1 weighted image were gradually brightened, and the T_1 map indicates the obvious shortening of their T_1

values (**Figure 3**a). Acquired by the linear-regression statistics shown in Figure 3b, the coefficient r_1 was 0.81 mM^{-1} s^{-1}, which showed a contrast-enhancement more than twice that of water-dispersible manganese oxide nanocrystals with a size of 7 nm, synthesized from the thermal decomposition of the Mn oleate complex (0.37 mM^{-1} s^{-1}).[4] The obtained MnO NCs were stabilized by hydrophilic polymer PVP without any additional capping surfactants for phase transfer, leading to more high-spin metal ions exposed on the surface than for conventional MnO-related MR contrast agents.[33]

Materials
Views
www.MaterialsViews.com

ADVANCED
FUNCTIONAL
MATERIALS
www.afm-journal.de
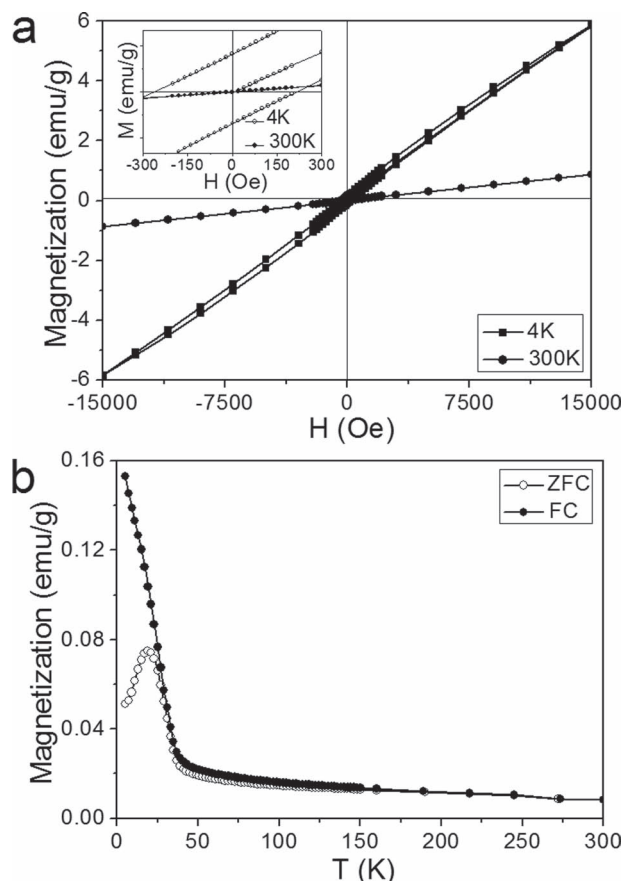
Figure 2. Magnetic behavior and magnetic resonance imaging ability of the MnO nanocrystals. a) M–H curves of MnO recorded at 4 K and 300 K. b) Magnetization curve of MnO nanocrystals versus temperature.

Based on the one-pot synthesis of the water-soluble MnO nanocrystals, it is facile to hybridize functional materials (silica, gold, graphene sheets, etc.) with MnO nanocrystals to obtain hydrophilic nanocomposites via their direct addition

into the reaction solution for microwave heating. Taking silica for example, MnO nanocrystals were absorbed onto the surface of silica nanosphere to form a continuous shell (Figure 3c inset). An obvious enhancement of the MR imaging effect was observed due to the self-assembly of MnO nanocrystals, and the longitudinal relaxivity (r_1) of the MnO@SiO$_2$ nanocomposites under lower magnetic field (0.47 T) was found to increase to 3.34 mM^{-1} s^{-1} in comparison with that under a 3.0 T magnetic field (1.34 mM^{-1} s^{-1}) (Figure 3c). This is in agreement with previously reported work, for example the HMnO@mSiO$_2$.[4]

2.3. Biocompatibility and Endocytosis

After incubation with HeLa-LC3 cells, a large number of MnO nanocrystals were found, in the Bio-TEM image of a cellular section, shown in **Figure 4**a to gather together in endosomes and the cytosol by efficient vesicular-mediated cellular uptake, due to charge surfactants and accelerated metabolism of cancer cells.[34] Efficient endocytosis of MnO nanocrystals into cancer cells should be conducive to MR detection with them as T_1 weighted contrast agents. Due to the paramagnetic manganese contrast enhancement, T_1-weighted MR images of the HeLa cells and HepG2 cells cultured with MnO nanocrystals at the concentration of 10 μg mL^{-1} showed a significant shortening of the T_1 relaxation time from 3375.3 and 2834.8 to 144.1 and 183.3 ms (Figure 4b,c).

Cell viability in response to different concentrations of MnO nanocrystals present in the culture media was evaluated by the 3-[4,5-dimethylthiazol-2-yl]-2,5-diphenyltetrazolium bromide (MTT) assay. As the concentration of MnO nanocrystals increased from 5 to 200 μg mL^{-1}, the viabilities of HeLa cells (a human epithelial carcinoma cell line) and HepG2 (Human hepatocellular liver-carcinoma cell line) cells were not remarkably altered after 24 h incubation, and only 19.78 ± 1.36% and 23.77 ± 1.70% decreases in HeLa and HepG2 cell viability were observed at high concentrations of even 200 μg mL^{-1} (Figure 4d), indicating that the MnO nanocrystals were promising for bioimaging and other biological applications. In comparison, a
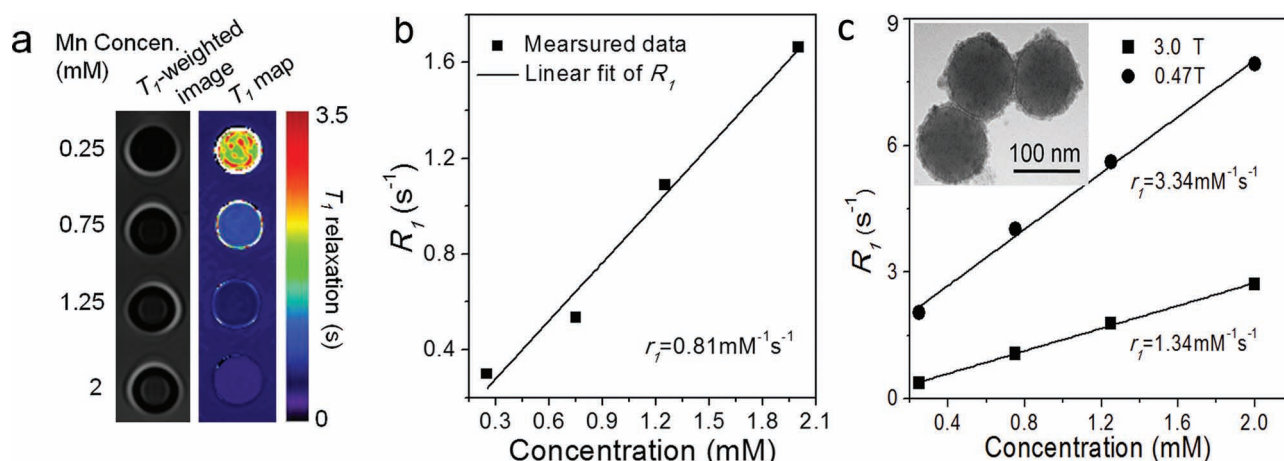
Figure 3. a) T_1-weighted image and T_1 map of MnO nanocrystals suspended in water at 3 T with concentration varying from 0.25 to 2 mM. b) Plot of R_1 ($1/T_1$) versus manganese concentration, and the slope indicates the longitude relaxivity (r_1) of the MnO nanocrystals. c) Plot of R_1 versus Mn concentration of the MnO@SiO$_2$ nanocomposites at 0.47 T and 3 T. The inset shows a TEM image of the MnO@SiO$_2$ nanocomposites.
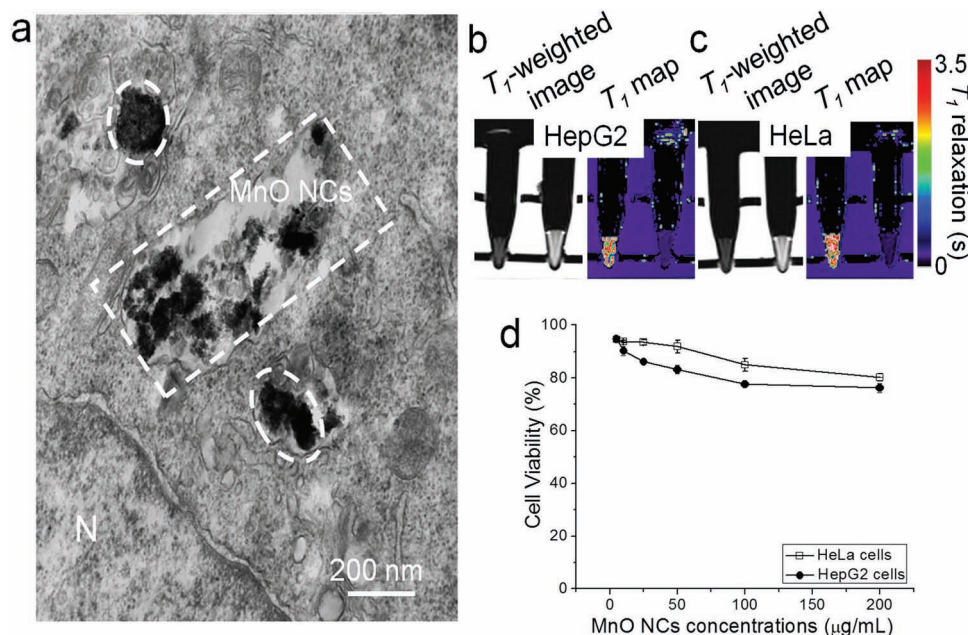
Figure 4. a) Bio-TEM images of HeLa-LC3 cells treated with MnO nanocrystals for 18 hours. The internalized nanocrystals were isolated, shown by the white dashed lines. b,c) T_1-weighted images and pseudocolor T_1 maps of HepG2 cells and HeLa cells after 24 h incubation with MnO nanocrystals. In each image, the left column is agarose gel with pure cells as a control. d) MTT cytotoxicity assay of HeLa cells and HepG2 cells exposed to varying concentrations of MnO nanocrystals.

relatively high cellular toxicity of manganese salt was reported previously by Mukhopadhyay and Linstedt[35] as the chief drawback for MEMRI. Therefore, converting toxic manganese ion into hydrophilic manganese oxide nanomaterials was a hopeful way of attacking this problem. In addition, no hemolysis was detected on exposure to MnO NCs at 100 µg mL^{-1}, and the hemolysis potential was $2.85 \pm 0.97\%$ that was obviously lower than the limit of 5%, demonstrating their potential blood compatibility for intravenous injection and blood circulation.
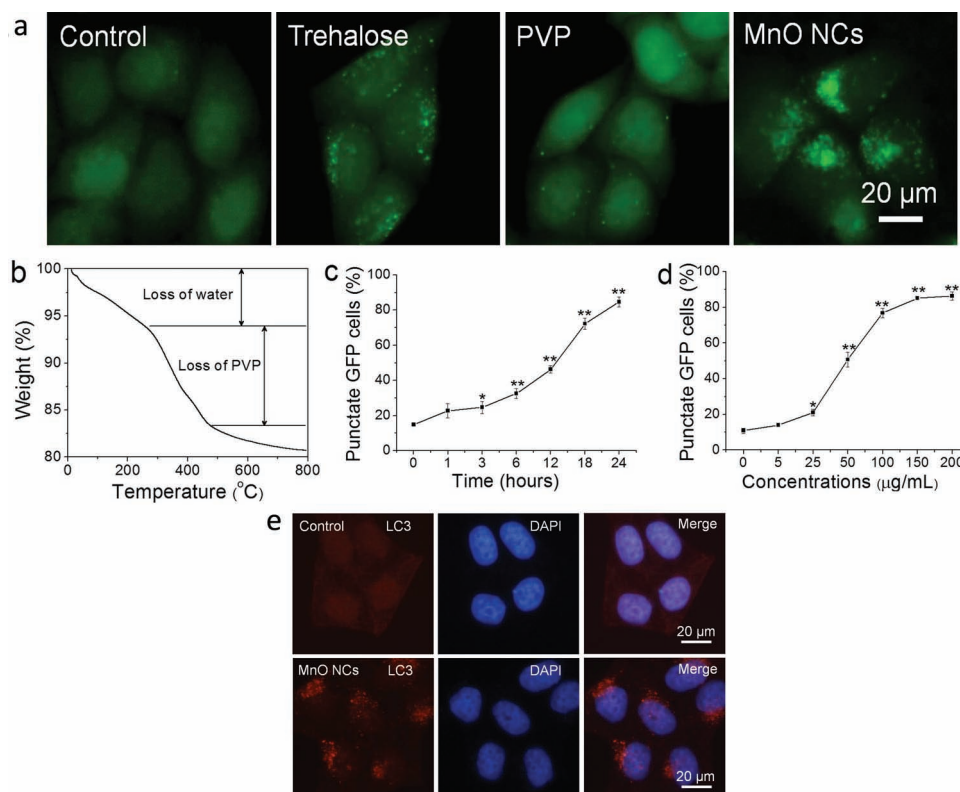
2.4. MnO Nanocrystals Induce LC3-Dot Formation

The autophagy-inducing effects of quantum dots (QDs),[36,37] gold,[38] and iron oxide nanoparticles[39] with special properties were documented in mammalian cells, which made some nanocrystals novel classes of autophagy activators.[40,41] To test the autophagy-inducing ability of MnO NCs, we established HeLa-GFP-LC3, a HeLa cell line stably expressing green-fluorescent-protein-tagged microtubule-associated protein 1 light chain 3 (GFP-MAP1LC3). This protein is normally diffusely present in the cytoplasm, but upon autophagy appears as green punctate dots.[42] We observed that after treatment of HeLa-LC3 cells with MnO nanocrystals, many green punctate dots appeared, compared with an evenly distributed green fluorescence in control cells (**Figure 5**a). Thermogravimetric (TG) analysis indicated that there was about 11 wt% weight loss of the as-prepared NPs from the decomposition of PVP (Figure 5b). Therefore, we treated HeLa-LC3 cells with 15 µg mL^{-1} PVP (a little more than the equal amount in the NCs) to confirm that the autophagic effect was induced by the nanocrystals but

not the surfactant (Figure 5a). Trehalose, a commonly used autophagy inducer, served as a positive control here. Upon treatment of HeLa-LC3 cells with MnO nanocrystals, LC3 dots positive cells continued to increase as time went by (Figure 5c). The effect of MnO NCs on the GFP-LC3 dot formation was also dose-dependent (Figure 5d). As shown in Figure 5e, the endogenously-expressed LC3 protein also exhibited a punctate pattern in the MnO NCs-treated cells. Collectively, these data demonstrated that MnO NCs induced LC3 dot formation, a hallmark feature of autophagy.

2.5. MnO Nanocrystals Induce Additional Autophagic Features

To lend more concrete proof that MnO NCs induced authentic autophagy, we present several additional lines of evidence. Autophagy was characterized by autophagosomes, consistent with their presumed autophagosome/autolysosome identity; most of the GFP-LC3 dots observed after MnO NCs treatment were stained by monodansylcadaverine (MDC), a dye that stains acidic vesicles (**Figure 6**a). Moreover, co-localization was extensively observed between the GFP-LC3 dots and Lyso-Tracker Red, a selective dye of the lysosome, strongly suggesting that these GFP-LC3 dots were probably autolysosomes (Figure 6a). Finally, a TEM study (Figure 6b) revealed that the HeLa cells treated with MnO NCs contained both autophagosomes and autolysosomes: early or initial autophagic vacuoles (AVi) containing morphologically intact cytoplasm constituents, and late or degradative autophagic vacuoles (AVd) containing partially degraded cytoplasmic materials, exhibiting increased electron density.[43]

www.MaterialsViews.com

ADVANCED
FUNCTIONAL
MATERIALS
www.afm-journal.de

FULL PAPER

Figure 5. Dot formation induced by MnO nanocrystals. a) GFP-LC3 dots formed in HeLa-LC3 cells treated with PBS (control), PVP (15 µg mL^{-1}), trehalose (100 mM), or MnO NCs (100 µg mL^{-1}) for 18 h. b) TGA curve of the as-prepared MnO nanocrystals. c,d) Time course (c) and dose-dependent (d) manner of GFP-LC3 dot formation in HeLa-LC3 cells treated with MnO NCs. e) HeLa cells treated with PBS or MnO NCs were analyzed with immunofluorescence (IF), and the nuclei are indicated by DAPI staining (mean ± standard error on the mean (s.e.m.), $n = 3$, *$p < 0.05$, **$p < 0.01$, compared with the control of each group).

Among the hallmarks to monitor the autophagic process, MAP1-LC3 (LC3) has so far been the best marker protein for autophagosomes.[44] LC3 is constitutively expressed in the cytosol and is immediately processed to form soluble LC3-I. When autophagy is induced, the newly generated carboxyl-group of LC3-I is transferred to phosphatidylethanolamine, generating autophagosomal membrane-bound LC3-II, which consequently exhibits a molecular-form conversion on Western blotting. As shown in Figure 6c, MnO NCs treatment resulted in an increase of the 16 kDa form (LC3-II),[45] but surfactant PVP failed to show the LC3-II increase. Furthermore, the amount of LC3-II increased in a time-dependent manner accompanied with dose-dependent manner (Figure 6d,e). Taken together, MnO NCs induced autophagy in HeLa cells. Furthermore, to certify the specificity of MnO NCs as MR contrast agents in the induction of autophagy, we have introduced iron oxide nanoparticles[46] with similar size and dextran[47] to compare their autophagy-induction abilities. As widely reported T_2-MR contrast agents, magnetite nanoparticles have been commercially used in clinical diagnosis (Feridex). Additionally, dextran is another important component of Feridex as the stabilizer. Herein, we have found that the best hallmark of autophagy, LC3, converted from LC3-I to the membrane-bound form LC3-II dramatically, indicating that MnO NCs induced more-powerful autophagy than either magnetite nanoparticles

or dextran, so our hydrophilic MnO nanocrystals possessed specific autophagy-induction potency to some extent, in comparison with the generally used MR contrast nanoagents (Supporting Information, Figure S1a).

2.6. MnO Nanocrystals Induce Genuine Autophagy by Enhancing Autophagosome Formation

Up to now, few investigations have been carried out in studying the autophagy phenomenon induced by magnetic nanocrystals, not to mention the detailed mechanism involved in the process. Autophagy is a dynamic process and some forms of autophagy are incomplete. For instance, calcium phosphate (CPP) induces autophagosome formation but also blocks autophagosome-lysosome fusion.[48] One of the best approaches to measure the rate of autophagy is bafilomycin A1 (Baf A1) treatment, which inhibits the vacuolar H$^+$-ATPase and prevents fusion between autophagosome and lysosome, leading to LC3-II degradation inhibition.[49] We discerned that the MnO NCs increased LC3-II levels significantly in the presence of Baf A1, strongly suggesting that MnO nanocrystals enhanced a new formation of autophagosome (**Figure 7**a). Besides Baf A1, chloroquine (CQ) is another classical lysosomotropic agent that perturbs lysosomal degradation by increasing the lysosomal pH.[50] In the presence

FULL PAPER
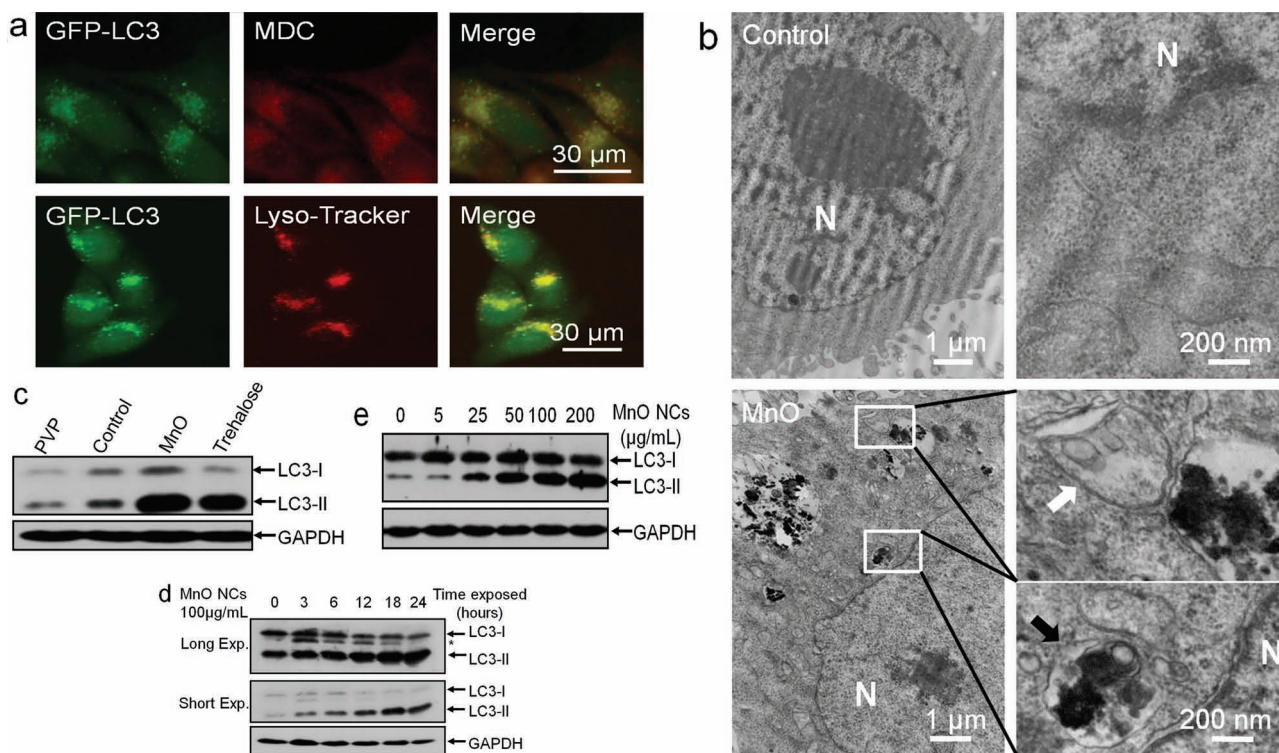
Figure 6. Additional autophagic features and LC3 conversion elicited by MnO nanocrystals. a) Fluorescent microscopy images of HeLa-LC3 cells treated with Lyso Tracker. b) Bio-TEM images of HeLa-LC3 cells treated with PBS or MnO nanocrystals. Typical AVi (white arrow) and AVd (black arrow) are indicated. c) HeLa cells were treated with PBS, PVP, MnO NCs or trehalose (100 mM). d,e) HeLa cells were treated with MnO NCs for the indicated hours (d) and various doses (e). (GAPDH served as a loading control. ∗ indicates non-specific bands).

of CQ, LC3-II increases in a time and dose-dependent manner in HeLa cells treated with MnO NCs (Supporting Information, Figure S1b,c).

Another valuable indicator for autophagic degradation is free GFP. When GFP-LC3 is delivered to a lysosome, the GFP part of the chimera is relatively resistant to hydrolysis. Therefore, the appearance of free GFP could be applied to monitor the breakdown of the cargo.[51] Flux analysis shows a much greater amount of the free GFP moiety in MnO NC-treated cells. Furthermore, the appearance of the free GFP moiety was suppressed efficiently by the saturating dose[51] of CQ (Figure 7b), indicating that at least a portion of autophagosomes were degraded in the lysosomes, together with the previous observation of the co-localization between GFP-LC3 aggregates and lysosomes (Figure 6a). In conclusion, MnO NC-induced authentic autophagy was literally or at least partially through the lysosomal stage.

2.7. Autophagy Induced by MnO Nanocrystals Is Not Dependent on p53 Activation

The tumor suppressor p53 is important not only in preventing tumorigenesis but also being involved in development, metabolism, and ageing.[52] Recently, it was reported that autophagy could be induced in either a p53-dependent or p53-independent manner.[53,54] The HeLa cell line is widely assumed to be

p53-defective, as p53 is continually compromised by the integrated human papilloma viral oncoprotein E6 through the ubiquitination pathway. Thus, it would be highly desirable to explore other cell lines for the intracellular signaling pathway study. We found that MnO NCs increased LC3-II levels significantly either in the presence or absence of CQ in HepG2, HaCat, and COS-7 cell lines (Supporting Information, Figure S2), indicating that autophagy occurrence was a common response of the cells to MnO nanocrystals.

Then, we employed the proper candidate HepG2 cell line[55] to evaluate the role of p53 in autophagy induction. As shown in Figure 7c, up-regulation of LC3-II was detected in MnO NCs-treated cells. Simultaneously, endogenous p53 and its transcriptional target p21[56] levels were both slightly increased, which argues that p53 activation occurred during the autophagy induction. Etoposide served as a positive reference here. The specific siRNA duplex targeted against p53[57] resulted in dramatic decline of p53 (Figure 7d), but as presented, the processed LC3-II levels showed no significant difference between the independent groups treated with p53 or control siRNA. These findings suggest that there was no perfect positive correlation between p53 transcriptional stimulatory activity and the autophagy level manifested by the MnO NCs. In other words, p53 activation should present an indirect effect on MnO NCs-mediated autophagy. Nevertheless, we should not exclude the possibility that slight activation of p53 after RNAi was still adequate for MnO NCs to elicit autophagy. Thus, we employed the

www.MaterialsViews.com

ADVANCED
FUNCTIONAL
MATERIALS
www.afm-journal.de

FULL PAPER
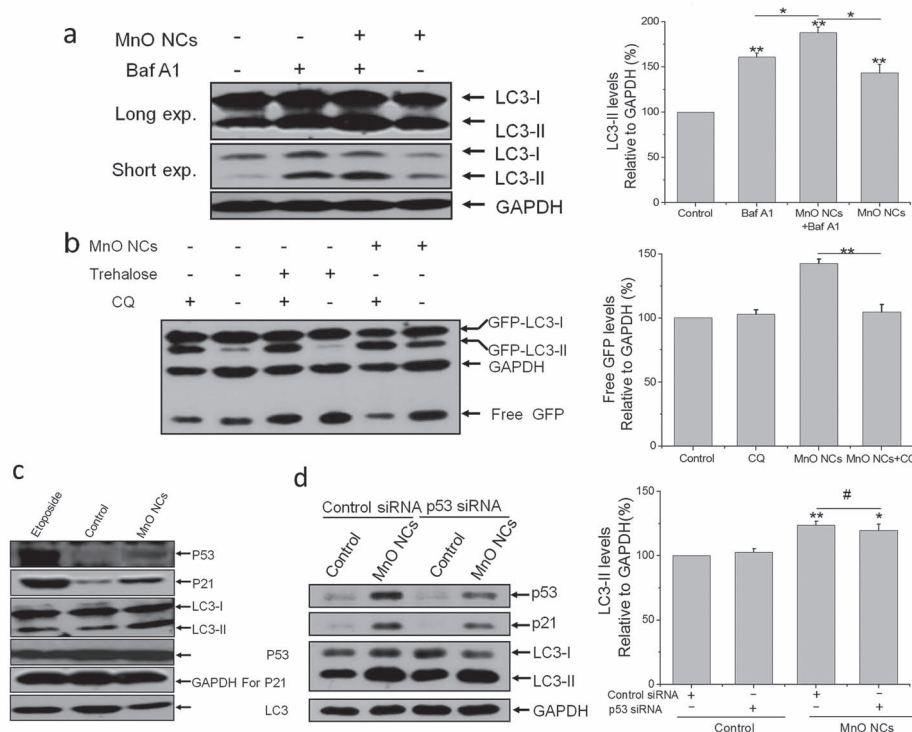
Figure 7. MnO NCs induce p53-independent autophagy by enhancing autophagosome formation. a) HeLa cells were treated with PBS or MnO NCs in the presence or absence of 400 nM bafilomycin A1 (added 4 h before cell harvest). b) HeLa-LC3 cells were either treated with PBS or MnO NCs in the presence or absence of 50 μM chloroquine. c) HepG2 cells were treated with PBS or MnO NCs and etoposide (50 μM) for 18 h. d) HepG2 cells, after transfection with control siRNA or p53 siRNA for 30 h, were treated with PBS or MnO NCs for 18 h. (In all of the experiments, protein levels were quantified by densitometric analysis relative to GAPDH. mean ± s.e.m., $n = 3$, $\#p > 0.05$, $*p < 0.05$, $**p < 0.01$, compared with the control of each group; the data are representative of three independent experiments with similar results).

human colon cancer p53$^{-/-}$ HCT116 cell line, in which p53 was knocked out by homologous recombination,[58] to investigate the autophagy induction of MnO NCs. In accordance with the previous results in HepG2 cells, MnO NCs could also induce autophagy regardless of the p53 level in p53$^{-/-}$ HCT116 cells (Supporting Information, Figure S3). Collectively, autophagy induced by MnO nanocrystals was not in a p53 transcription-dependent manner.

2.8. Enhanced Autophagy Contributes to the Synergetic Effect of MnO Nanocrystals and Doxorubicin on Killing Cancer Cells In Vitro and In Vivo

As shown in Figure 4d, MnO NCs present good biocompatibility according to the results of cell-viability assay and hemolysis analysis, but we still managed to improve their safety a step further by modulating the autophagy behavior of this novel T_1-MRI contrast agent. Recently, it has been postulated that excessive or aberrant autophagy caused by PAMAM G3 or single-walled carbon nanotubes (SWCNTs) directly promotes cell death.[59,60] We introduced 3-methylamphetamine (3-MA) to test whether the cell-viability decrease caused by MnO nanocrystals is also prevented by autophagy inhibition. As a potent inhibitor of autophagy via the depression of PtdIns3-kinase activity, 3-MA blocks the formation of autophagosomes

without affecting intracellular protein synthesis.[44,61] Co-treatment with 3-MA significantly reduced LC3 puncta formation (**Figure 8**a) and the endogenous LC3-II levels (Figure 8b) induced by the MnO NCs. Meanwhile, we found that the viability decrease and death-rate increase of HeLa cells after MnO treatment detected by MTT assay (Supporting Information, Figure S4a) and Hoechst 33342/propidium iodide (HO/PI) staining (Figure 8c) could be significantly reversed by 3-MA treatment. Wortmannin, another widely used specific inhibitor of autophagy,[62] also executed the rescue effect to improve the biocompatibility of MnO NCs. The similar re-establishment of the cell viability by 3-MA in HepG2 cells was also observed (Supporting Information, Figure S4b–d). These results illustrated that autophagy has played a crucial role specifically in MnO NCs-induced cell death.

Doxorubicin (Dox) is commonly applied as a front-line chemotherapeutic agent to treat a wide range of cancers by inducing apoptosis via activation of caspase-3 and other caspases.[63] In accordance with these published reports, Dox at a relatively high dose caused apoptosis in a caspase-mediated manner (Supporting Information, Figure S5) and rigorously killed cancer cells (data not shown). However, it has been addressed that various multidrug resistance cells appeared to attenuate apoptosis.[64,65] Moreover, extremely high doses of Dox should lead to severe perturbations and side effects such as heart damage, nausea, hair loss, and so on.[66] In this context,
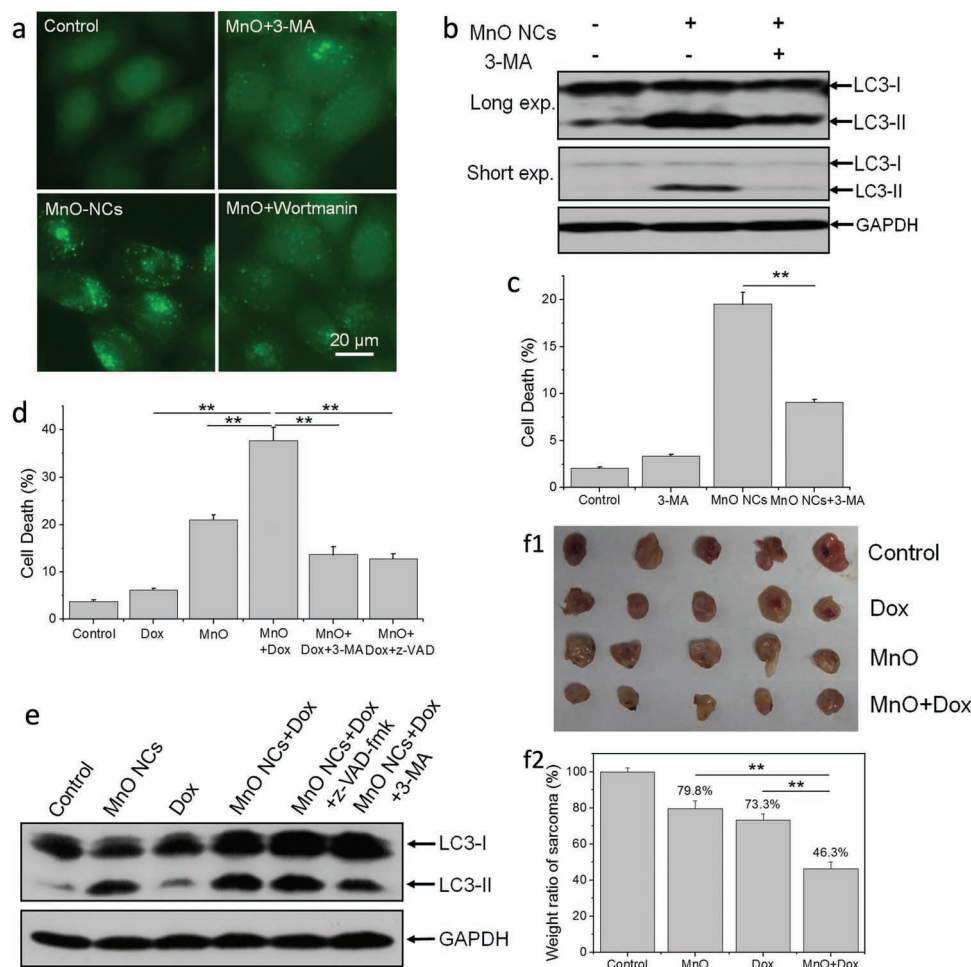
Figure 8. MnO nanocrystals and doxorubicin co-treatment executes a synergistic effect on cancer therapy, which might be mediated by autophagy induction. a) GFP-LC3 dot formation of HeLa-LC3 cells either treated with PBS, MnO NCs, MnO NCs plus 3-methyladenine (2.5 mM), or Wortmannin (0.5 μM) separately. b) HeLa cells were either treated with PBS or MnO NCs and MnO NCs plus 3-MA. c) Cell-death assay of HeLa cells after treatment with PBS, MnO NCs, MnO NCs plus 3-MA, and 3-MA only. d,e) Cell-death assay (d) and Western blotting analysis (e) of HeLa cells, which were treated with Dox (0.75 μg mL^{-1}), MnO NCs alone, MnO NCs plus Dox, or MnO NCs-Dox co-treated with 3-MA or z-VAD-fmk (20 μM). (Cell death was assessed by Hoechst 33342/PI staining and PI-positive cells are expressed as a percentage of the total number of cells. mean ± s.e.m., $n = 3$, **$p <$ 0.01; The data are representative of three independent experiments with similar results). f1,f2) Synergistic killing effect in murine S180 tumor model. Photo (f1) and weight ratio (f2) of tumor tissues from mice treated with normal saline (NS), 2 mg kg^{-1} Dox, 4 mg kg^{-1} MnO NCs or Dox plus MnO NCs. mean ± s.e.m., $n = 5$, **$p < 0.01$.

it would be highly desirable to develop novel and effective anticancer drugs for chemotherapy, especially available in co-operation with a nontoxic dose of Dox. As mentioned above, MnO NCs could induce autophagic cell death, which was not so dependent on the apoptotic pathway, and it might be of great value in the treatment of cancer cells that show little response to conventional chemotherapeutics such as doxorubicin. As expected, we observed that combined treatment of 100 μg mL^{-1} MnO NCs and Dox at the non-cytotoxic concentration of 0.75 μg mL^{-1}[29] resulted in 37.72 ± 2.77% death of HeLa cells, while the same dose of Dox and MnO NCs alone rarely caused so significant cell death (Figure 8d, Supporting Information, Figure S6). To conduct further investigation into the role of MnO NCs in enhancing the tumoricidal effect by modulating the autophagy event, we treated HeLa cells with MnO NCs and Dox in the presence of 3-MA or z-VAD-fmk, a cell-permeable

pan caspase inhibitor. It was shown that an enhanced chemotherapy efficacy was almost invalid when MnO NCs plus Dox were coadministrated with 3-MA (Figure 8d and Supporting Information, Figure S6). Accordingly, 3-MA succeeded in inhibiting the autophagy induction from combined treatment HeLa cells with MnO NCs and Dox (Figure 8e). We naturally tended towards the speculation that the autophagic potency originating from the MnO NCs might greatly contribute to the synergistic tumor-killing effect. Notably, z-VAD-fmk also made synergistic killing vanish (Figure 8d and Supporting Information, Figure S6), although it failed to alter the autophagy level elicited by the MnO NCs coadministrated with Dox, revealed by the negligible decrease of the endogenous LC3-II levels of MnO NCs-Dox-treated HeLa cells (Figure 8e). These results strongly suggest that autophagy should not be the terminal executor, but is definitely the vital participant of the enhanced killing effect.

Materials
Views

www.MaterialsViews.com

ADVANCED
FUNCTIONAL
MATERIALS
www.afm-journal.de

FULL PAPER

Further work is highly desirable to address the definite signaling pathways involved in the synergetic killing effect of MnO NCs and Dox, as autophagy has so many and frequent crosstalk with apoptosis or necrosis.[67]

Finally, to assess the synergistic killing effect of MnO NCs and Dox in vivo, we introduced the Sarcoma 180 (S180) tumor-bearing mice[68,69] by inoculated subcutaneously (s.c.) the ascites in the right forelimb. All of the 20 mice were randomly divided into four groups, a control group, a Dox group, a MnO NCs group and a MnO NCs + Dox group. The mice received each administration every other day. Dox was injected intraperitoneally (i.p.) at a concentration of 2 mg kg^{-1}, and 4 mg kg^{-1} MnO NC solution was injected subcutaneously (s.c.) into the tumor of each mouse. The control group received an injection of the same amount of normal saline (NS) solution intraperitoneally and subcutaneously, respectively. All of the mice were sacrificed after three drug administrations, and the subcutaneous sarcoma tumors were peeled off, photographed, and weighed. The data show that Dox or MnO NCs alone could only reduce 26.65 ± 3.31% and 20.24 ± 4.10% of the tumor weight, compared with that of the NS-treated group; however, MnO NCs in combination with Dox had a confirmative synergistic tumoricidal effect, as the co-drug treatment group led to a 53.66 ± 3.65% tumor-weight decrease (Figure 8f). Collectively, our results confirm that MnO NCs combined with lower and non-cytotoxic concentration of Dox simultaneously could have a significant synergistic effect in killing the cancer cells. Notably, in accordance with previous data in vitro, the synergistic killing effect in vivo was also not merely the additive effect of the two drugs, which provides new insight for combinatorial chemotherapy of multiple cancers by enhancing the autophagy levels.

3. Conclusions

In summary, hydrophilic MnO nanocrystals with good biocompatibility can be synthesized in a microwave-assisted polyalcohol system for the first time. The advantages of the obtained MnO nanocrystals serving as excellent MR imaging agents include their hydrophilic surface, ligand-modification-free, and facile fabrication of biological functionalized manganese oxide nanocomposites. Furthermore, we found that MnO nanocrystals can induce authentic functional autophagy by enhancing autophagosome formation without disturbing the fusion between autophagosomes and lysosomes, and the autophagic effect elicited by MnO nanocrystals was also revealed in a p53-activation independent manner. Eventually, co-treatment with MnO nanocrystals and doxorubicin led to a significant synergistic effect in killing cancer cells, and the preliminary proof demonstrates that MnO NCs mediated the synergistic tumoricidal effect through autophagy modulation.

Many more studies are still highly desirable to elucidate the crosstalk between autophagy and apoptosis or necrosis[67] involved in the synergistic effect, and to explore more clinical applications of the autophagy induced by MnO nanocrystals, such as the clearance of mutant proteins and pathogen elimination. Although it has been reported that poly(vinyl pyrrolidone) (PVP) can increase the circulation time in vivo to enhance passive tumor targeting of nanoparticles via an enhanced permeation and retention (EPR) effect, modification of synthesized PVP molecules such as xanthate-mediated reverse addition fragment transfer (RAFT) will generate thiol, hydroxyl, and aldehyde functional groups to conjugate folate, transferrin, Her2/neu receptor antibody, chlorotoxin (CTX), and several other peptides for active targeted imaging and therapy.[70–72] In addition, layer-by-layer (LbL) assembly of charged polymers and encapsulation of inorganic shells such as silica, gold, and rare earth metals also provide promising opportunities for bioconjugation and mutlifunctionality.[4–8,73,74] There is no doubt that understanding and modulating autophagy elicited by MnO nanocrystals should ultimately allow us to improve human health in clinical applications of MnO nanocrystals. There is no doubt that understanding and modulating autophagy should be essential to the clinical applications of MnO nanocrystals.

4. Experimental Section

Materials: Manganese (II) 2,4-pentanedionate (Mn(acac)$_2$) and manganese (III) 2,4-pentanedionate (Mn(acac)$_3$) were purchased from Alfa Aesar; poly(vinyl pyrrolidone) (PVP, M_w = 40 000 g mol^{-1}), triethylene glycol (TREG), and tetraethylorthosilicate (TEOS) were purchased from the Shanghai Reagent Company (P. R. China). Trehalose (T9531), monodansylcadaverine (MDC) (D4008), Wortmannin (W1628), 4′,6-diamidino-2-phenylindole (DAPI) (D8417), 3-methyladenine (08592), doxorubicin (D1515), etoposide (E1383), bafilomycinA1 (B1793), N-benzyloxycarbonyl-Val-Ala-Asp(O-Me) fluoromethyl ketone (z-VAD-fmk,V116), chloroquine (C6628), propidium iodide (PI) (P4864) and Hoechst 33342 (HO,B2261) were all purchased from Sigma–Aldrich (St. Louis, MO). Lyso Tracker Red (L7528), lipofectamine 2000 (11668-019) and oligofectamine (12252-011) were all purchased from Invitrogen (Carlsbad, CA). 3-[4,5-dimethylthiazol-2-yl]-2,5-diphenyltetrazolium bromide (MTT) (TB0799) was from Sangon Biotechnology (P. R. China). LC3 antibodies (NB100-2220) were purchased from Novus (Littleton, CO). GFP (sc-101536) and p53 (sc-126) antibodies were from Santa Cruz Biotechnology. The p21 antibodies (556430) were from BD Biosciences. Cleaved caspase 3 antibodies were purchased from Beyotime Institute of Biotechnology (P. R. China) and glyceraldehyde phosphate dehydrogenase (GAPDH) antibodies (AB9132) were from Chemicon. HRP-conjugated anti-rabbit (W4011) and anti-mouse (W4021) antibodies were purchased from Promega (Wisconsin, USA). Enhanced chemiluminescence (ECL) kits were from Biological Industries (Kibbutz beit Haemek, Israel).

Microwave-Assisted Synthesis of MnO Nanocrystals: In a typical procedure, analytically pure Mn(acac)$_2$ (0.5 mmol) and PVP (0.6 g) were added into a flask in the presence of 15 mL of TREG solution. After stirring the solution for half an hour in a 135 °C oil bath, the transparent brown solution was quickly transferred into a quartz tube for the following microwave synthesis. The microwave tube was sealed and maintained in a single-mode microwave synthesis system (Discovery, CEM Corp, USA) under 260 °C for 10 minutes with a heating power of 200 W, and then quickly cooled down to room temperature using an air-compressor pump. The obtained dark-brown solution was then centrifuged, washed several times with ethanol and deionized water to remove ions and possible remnants. The manganese concentration was measured by inductively coupled plasma atomic emission spectroscopy (ICP-AES) (Optima 7300 DV, Perkin–Elmer Corp, USA) for further characterization.

Characterization: The samples were characterized by X-Ray powder diffraction, scanning electron microscopy (JSM-6700F), transmission electron microscopy (JEOL-2010), and superconducting quantum interface device (SQUID) magnetometer (Quantum Design MPMS XL) measurements.

Magnetic Resonance Imaging (MRI): All of the plastic tubes with the MnO nanocrystals solution and gel were immersed in NiSO$_4$ solution

for MR analysis. For r_1 measurement of the obtained MnO nanocrystals with a 3 T clinical MRI scanner (Siemens, Tim Trio) containing a knee coil, the turbo spin echo (TSE) sequence was used: repetition time (T_R): 300, 500, 700, 900 ms; echo time (T_E): 7.4 ms; field of view (FOV): 192 mm × 220 mm. Then, the data were exploited to fit non-linearly with the equation $M(T_R) = M_0 (1 - \exp(-T_R/T_1))$ to calculate the T_1 values at different concentrations. Finally, the r_1 value was obtained by linear regression. Longitudinal relaxation time (T_1) measurements of MnO@ SiO_2 nanospheres were also performed on a 0.47 T NMI20-Analyst (Niumag Corp., Shanghai, P. R. China) by an inversion-recovery (IR) pulse sequence. For T_1-weighted cellular imaging, the TSE sequence was used: $T_R = 400$, 600 ms, $T_E = 16$ ms.

Cell Culture and Establishment of HeLa-GFP-LC3 Cell Line: All of the cell lines were cultured in Dulbecco's modified Eagle's medium (DMEM). To develop the stable transfected cell line, HeLa cells were transfected with pGFP-LC3 plasmid and then selected via 600 μg mL^{-1} G418 for 10 days.

GFP-LC3 Dots Formation Assay: Under fluorescence microscopy, GFP-LC3 dots were quantified by counting more than 300 cells. The assays were independently performed by two of the authors in a double-blind manner.

Autophagic Marker Dye Staining: HeLa-LC3 cells, after MnO NCs treatment, were treated for 15 min with 10 μM monodansylcadaverine (MDC) or 75 nM Lyso Tracker Red. After washing twice with PBS, the cells were examined under fluorescence microscopy (Olympus IX71).

Immunofluorescence: HeLa cells were fixed by 4% paraformaldehyde in PBS for 10 minutes and permeabilized with 0.5% Triton X-100 for another 10 minutes. After blocking with 5% fetal bovine serum (FBS) for 1 hour, cells were incubated with LC3 antibodies for 2 hours at room temperature (RT) and then detected with rhodamine (Red)-conjugated secondary antibody followed by incubation with DAPI for 5 minutes.

Cell-Death Assay: For Hoechst 33342/PI staining assay, cells were stained with Hoechst 33342 (20 μg mL^{-1}) and PI (10 μg mL^{-1}) for 10 min and then examined under fluorescence microscopy (Olympus IX71). Cell death was quantified by counting at least 500 cells in triplicate for each experimental condition, and the results were expressed by the percentage of PI-positive cells to the total number of cells (Hoechst positive cells). The assays were independently performed by two of the authors in a double-blind manner.

Western Blotting Analysis: Briefly, cells were cultured in 24-well plates to approximately 80% of confluence and treated with various compounds. After harvesting via trysinization at the indicated times, cell pellets were resuspended with the lysis buffer (0.5% Nonidet P-40/10 mM Tris-HCl, pH 7.5/100 mM NaCl) supplemented with a protease inhibitor cocktail on ice. An equal volume of 2× sodium dodecyl sulfate (SDS) sample loading buffer (100 mM Tris-HCl, pH 6.8, 2% β-mercaptoethanol, 4% SDS, 20% glycerol, and 0.02% Bromphenol blue) was added, followed by boiling for 10–15 minutes. Proteins were separated on a 12%–15% SDS-polyacrylamide gel electrophoresis (SDS-PAGE) gel and transferred to nitrocellulose membrane (GE Healthcare Life Sciences). After blocking with Tris-buffered saline (TBS) containing 0.1% polyoxyethylene (20) sorbitan monolaurate (Tween-20) and 5% nonfat dry milk, the nitrocellulose membrane was incubated overnight at 4 °C with a primary antibody at an appropriate dilution (1:2000-1:1000), extensively washed more than five times for 10 minutes each with TBST (TBS containing 0.1% Tween-20), incubated with HRP-conjugated secondary antibody (1:10 000 dilution) for 1 hour at RT, extensively washed and finally visualized using an ECL kit.

siRNA Transfection: HepG2 cells were incubated overnight in 24-well (1.0–1.5 × 10^5) plate in DMEM containing 10% FBS. When the cells were at 55–65% confluence the next day, the medium was replaced with fresh Opti-MEM containing 30.0 nM Control siRNA (Sense5′-UUCUCCGAACGUGUCACGUdTdT-3′; Antisense5′-ACGUGACACGUUCGGAGAAdTdT-3′) (Shanghai GenePharma Biotechnology, P. R. China) or an equal amount of p53 siRNA (Sense5′-CUACUUCCUGAAAACAACGdTdT-3′; Antisense5′-CGUUGUUUUCAGGAAGUAGdTdT-3′) and oligofectamine following the manufacturer's protocol exactly.

Animals and Tumor Model: Healthy Kunming male mice, aged 6–8 weeks, were purchased from the Experimental Animal Center of Anhui Medical University. Animal welfare and experimental procedures were carried out in accordance with the Ethical Regulations on the Care and Use of Laboratory Animals of University of Science and Technology of China and were approved by the school committee for animal experiments. For the tumor-model establishment, the ascitic cells were collected under sterile conditions and mixed together with saline to prepare a cell suspension at a concentration of 10^6 cells per mL, and then inoculated subcutaneously (s.c.) (0.2 mL) in the right forelimb. The 20 mice were randomly divided into four groups: a control group, a Dox group, a MnO NCs group and a MnO NCs + Dox group for the in vivo investigation of the synergistic chemotherapy effect. After the subcutaneous S180 ascites injection, the mice received MnO and Dox for chemotherapy at the second, fourth, and sixth days. Dox was injected intraperitoneally and MnO nanocrystal solution was injected subcutaneously into the tumor of each mouse. The control group received an injection of the same amount of normal saline solution intraperitoneally and subcutaneously, respectively. One week later, all of the mice were sacrificed and the stripped subcutaneous sarcoma tumors were weighed to evaluate the anti-tumor effect.

Statistical Analysis: All of the data were expressed as mean ± s.e.m. and analyzed by two-tailed student's t-tests. $*p < 0.05$ and $**p < 0.01$ were considered statistically significant.

Supporting Information

Supporting Information is available from the Wiley Online Library or from the author. Specific autophagy induction of MnO, autophagic effects of MnO in several cell lines, cell-viability rescue effects by specific inhibitors of autophagy and fluorescence images of PI staining are available.

Acknowledgements

[1] R. Hao, R. J. Xing, Z. C. Xu, Y. L. Hou, S. Gao, S. H. Sun, *Adv. Mater.* **2010**, *22*, 2729.

[2] J. H. Gao, H. W. Gu, B. Xu, *Acc. Chem. Res.* **2009**, *42*, 1097.

[3] J. Cheon, J. H. Lee, *Acc. Chem. Res.* **2008**, *41*, 1630.

[4] T. Kim, E. Momin, J. Choi, K. Yuan, H. Zaidi, J. Kim, M. Park, N. Lee, M. T. McMahon, A. Quinones-Hinojosa, J. W. M. Bulte, T. Hyeon, A. A. Gilad, *J. Am. Chem. Soc.* **2011**, *133*, 2955.

[5] Y. D. Jin, C. X. Jia, S. W. Huang, M. O'Donnell, X. H. Gao, *Nat. Commun.* **2010**, *1*, 41.

[6] Y. Lu, Y. Zhao, L. Yu, L. Dong, C. Shi, M. J. Hu, Y. J. Xu, L. P. Wen, S. H. Yu, *Adv. Mater.* **2010**, *22*, 1407.

[7] T. D. Schladt, M. I. Shukoor, K. Schneider, M. N. Tahir, F. Natalio, I. Ament, J. Becker, F. D. Jochum, S. Weber, O. Kohler, P. Theato, L. M. Schreiber, C. Sonnichsen, H. C. Schroder, W. E. G. Muller, W. Tremel, *Angew. Chem. Int. Ed.* **2010**, *49*, 3976.

[8] Y. Lu, C. Shi, M. J. Hu, Y. J. Xu, L. Yu, L. P. Wen, Y. Zhao, W. P. Xu, S. H. Yu, *Adv. Funct. Mater.* **2010**, *20*, 3701.

[9] H. B. Na, I. C. Song, T. Hyeon, *Adv. Mater.* **2009**, *21*, 2133.

[10] O. Veiseh, J. W. Gunn, M. Q. Zhang, *Adv. Drug Delivery Rev.* **2010**, *62*, 284.

[11] S. Laurent, D. Forge, M. Port, A. Roch, C. Robic, L. V. Elst, R. N. Muller, *Chem. Rev.* **2008**, *108*, 2064.

[12] M. J. Hu, Y. Lu, S. Zhang, S. R. Guo, B. Lin, M. Zhang, S. H. Yu, *J. Am. Chem. Soc.* **2008**, *130*, 11606.

[13] S. H. Sun, *Adv. Funct. Mater.* **2006**, *18*, 393-403.

[14] W. S. Seo, J. H. Lee, X. M. Sun, Y. Suzuki, D. Mann, Z. Liu, M. Terashima, P. C. Yang, M. V. McConnell, D. G. Nishimura, H. J. Dai, *Nat. Mater.* **2006**, *5*, 971.

[15] A. C. Silva, J. H. Lee, L. Aoki, A. R. Koretsky, *NMR Biomed.* **2004**, *17*, 532.

[16] H. B. Na, J. H. Lee, K. An, Y. I. Park, M. Park, I. S. Lee, D.-H. Nam, S. T. Kim, S.-H. Kim, S.-W. Kim, K.-H. Lim, K.-S. Kim, S.-O. Kim, T. Hyeon, *Angew. Chem. Int. Ed.* **2007**, *46*, 5397.

[17] M. I. Shukoor, F. Natalio, M. N. Tahir, M. Wiens, M. Tarantola, H. A. Therese, M. Barz, S. Weber, M. Terekhov, H. C. Schroder, W. E. G. Muller, A. Janshoff, P. Theato, R. Zentel, L. M. Schreiber, W. Tremel, *Adv. Funct. Mater.* **2009**, *19*, 3717.

[18] J. M. Shin, R. M. Anisur, M. K. Ko, G. H. Im, J. H. Lee, I. S. Lee, *Angew. Chem. Int. Ed.* **2009**, *48*, 321.

[19] M. U. Hutchins, D. J. Klionsky, *J. Biol. Chem.* **2001**, *276*, 20491.

[20] B. Levine, D. J. Klionsky, *Dev. Cell* **2004**, *6*, 463.

[21] S. Sarkar, D. C. Rubinsztein, *Mol. Biosyst.* **2008**, *4*, 895.

[22] N. Mizushima, T. Yoshimori, B. Levine, *Cell* **2010**, *140*, 313.

[23] N. Mizushima, B. Levine, A. M. Cuervo, D. J. Klionsky, *Nature* **2008**, *451*, 1069.

[24] D. C. Rubinsztein, M. Guillermo, G. Kroemer, *Cell* **2011**, *146*, 682.

[25] Y. Kondo, T. Kanzawa, R. Sawaya, S. Kondo, *Nat. Rev. Cancer* **2005**, *5*, 726.

[26] B. Levine, *Nature* **2007**, *446*, 745.

[27] B. Levine, J. Y. Yuan, *J. Clin. Invest.* **2005**, *115*, 2679.

[28] Y. J. Zhang, F. Zheng, T. L. Yang, W. Zhou, Y. Liu, N. Man, L. Zhang, N. Jin, Q. Q. Dou, Y. Zhang, Z. Q. Li, L. P. Wen, *Nat. Mater.* **2012**, *11*, 817.

[29] X. M. Wan, F. Zheng, L. Zhang, Y. Y. Miao, N. Man, L. P. Wen, *Int. J. Cancer* **2011**, *129*, 1087.

[30] M. Yin, S. O'Brien, *J. Am. Chem. Soc.* **2003**, *125*, 10180.

[31] Y. W. Jun, J. H. Lee, J. Cheon, *Angew. Chem. Int. Ed.* **2008**, *47*, 5122.

[32] W. S. Seo, H. H. Jo, K. Lee, B. Kim, S. J. Oh, J. T. Park, *Angew. Chem. Int. Ed.* **2004**, *43*, 1115.

[33] J. Huang, J. Xie, K. Chen, L. H. Bu, S. Lee, Z. Cheng, X. G. Li, X. Y. Chen, *Chem. Commun.* **2010**, *46*, 6684.

[34] H. T. Song, J. S. Choi, Y. M. Huh, S. Kim, Y. W. Jun, J. S. Suh, J. Cheon, *J. Am. Chem. Soc.* **2005**, *127*, 9992.

[35] S. Mukhopadhyay, A. D. Linstedt, *Proc. Natl. Acad. Sci. USA* **2011**, *108*, 858.

[36] O. Seleverstov, O. Zabirnyk, M. Zscharnack, L. Bulavina, M. Nowicki, J. M. Heinrich, M. Yezhelyev, F. Emmrich, R. O'Regan, A. Bader, *Nano Lett.* **2006**, *6*, 2826.

[37] S. T. Stern, B. S. Zolnik, C. B. McLeland, J. Clogston, J. W. Zheng, S. E. McNeil, *Toxicol. Sci.* **2008**, *106*, 140.

[38] X. W. Ma, Y. Y. Wu, S. B. Jin, Y. Tian, X. N. Zhang, Y. L. Zhao, L. Yu, X. J. Liang, *ACS Nano* **2011**, *5*, 8629.

[39] M. I. Khan, A. Mohammad, G. Patil, S. A. H. Naqvi, L. K. S. Chauhan, I. Ahmad, *Biomaterials* **2012**, *33*, 1477.

[40] O. Zabirnyk, M. Yezhelyev, O. Seleverstov, *Autophagy* **2007**, *3*, 278.

[41] F. Zhao, Y. Zhao, Y. Liu, X. L. Chang, C. Y. Chen, Y. L. Zhao, *Small* **2011**, *7*, 1322.

[42] Y. Kabeya, N. Mizushima, T. Uero, A. Yamamoto, T. Kirisako, T. Noda, E. Kominami, Y. Ohsumi, T. Yoshimori, *EMBO J.* **2000**, *19*, 5720.

[43] E. L. Eskelinen, *Autophagy* **2005**, *1*, 1.

[44] D. J. Klionsky, and 231 others, *Autophagy* **2008**, *4*, 151.

[45] N. Mizushima, T. Yoshimori, *Autophagy* **2007**, *3*, 542.

[46] A. Senpan, S. D. Caruthers, I. Rhee, N. A. Mauro, D. P. J. Pan, G. Hu, M. J. Scott, R. W. Fuhrhop, P. J. Gaffney, S. A. Wickline, G. M. Lanzat, *ACS Nano* **2009**, *3*, 3917.

[47] C. Claire, R. Philippe, I. Jean-Marc, P. Marc, *Adv. Drug Delivery Rev.* **2006**, *58*, 1471.

[48] S. Sarkar, V. Korolchuk, M. Renna, A. Winslow, D. C. Rubinsztein, *Autophagy* **2009**, *5*, 307.

[49] D. C. Rubinsztein, A. M. Cuervo, B. Ravikumar, S. Sarkar, V. Korolchuk, S. Kaushik, D. J. Klionsky, *Autophagy* **2009**, *5*, 585.

[50] S. N. Chen, S. K. Rehman, W. Zhang, A. D. Wen, L. B. Yao, J. A. Zhang, *Bichim. Biophys. Acta, Rev. Cancer* **2010**, *1806*, 220.

[51] H. M. Ni, A. Bockus, A. L. Wozniak, K. Jones, S. Weinman, X. M. Yin, W. X. Ding, *Autophagy* **2011**, *7*, 188.

[52] B. Levine, J. Abrams, *Nat. Cell Biol.* **2008**, *10*, 637.

[53] Z. H. Feng, H. Zhang, A. J. Levine, S. Jin, *Proc. Natl. Acad. Sci. USA* **2005**, *102*, 8204.

[54] W. M. Abida, W. Gu, *Cancer Res.* **2008**, *68*, 352.

[55] J. Bai, A. I. Cederbaum, *J. Pharmacol. Exp. Ther.* **2006**, *319*, 1435.

[56] W. S. El-Deiry, *Semin. Cancer Biol.* **1998**, *8*, 345.

[57] J. Wang, M. Y. Chin, G. Li, *Cancer Res.* **2006**, *66*, 1906.

[58] P. Jiang, W. J. Du, X. W. Wang, A. Mancuso, X. Gao, M. Wu, X. L. Yang, *Nat. Cell Biol.* **2011**, *13*, 310.

[59] C. G. Li, H. L. Liu, Y. Sun, H. L. Wang, F. Guo, S. A. Rao, J. J. Deng, Y. L. Zhang, Y. F. Miao, C. Y. Guo, J. Meng, X. P. Chen, L. M. Li, D. S. Li, H. Y. Xu, H. Wang, B. Li, C. Y. Jiang, *J. Mol. Cell Biol.* **2009**, *1*, 37.

[60] H. L. Liu, Y. L. Zhang, N. Yang, Y. X. Zhang, X. Q. Liu, C. G. Li, Y. Zhao, Y. G. Wang, G. G. Zhang, P. Yang, F. Guo, Y. Sun, C. Y. Jiang, *Cell Death Dis.* **2011**, *2*, e159.

[61] C. Takatsuka, Y. Inoue, K. Matsuoka, Y. Moriyasu, *Plant Cell Physiol.* **2004**, *45*, 265.

[62] E. F. Blommaart, U. Krause, J. P. Schellens, H. Vreeling-Sindelarova, A. J. Meijer, *Eur. J. Biochem.* **1997**, *243*, 240.

[63] S. Gamen, A. Anel, P. Lasierra, M. A. Alava, M. J. MartinezLorenzo, A. Pineiro, J. Naval, *FEBS Lett.* **1997**, *417*, 360.

[64] D. Kim, E. S. Lee, K. T. Oh, Z. G. Gao, Y. H. Bae, *Small* **2008**, *4*, 2043.

[65] J. N. Shen, Q. J. He, Y. Gao, J. N. Shi, Y. P. Li, *Nanoscale* **2011**, *10*, 4314.

[66] J. J. Monsuez, J. C. Charniot, N. Vignat, J. Y. Artigou, *Int. J. Cardiol.* **2010**, *144*, 3.

[67] M. C. Maiuri, E. Zalckvar, A Kimchi, G. Kroemer, *Nat. Rev. Mol. Cell Biol.* **2007**, *8*, 741.

[68] X. J. Yan, H. M. Chen, X. L. Lu, F. Wang, W. F. Xu, H. X. Jin, P. Zhu, *Eur. J. Pharm. Sci.* **2011**, *43*, 251.

[69] X. L. Liu, N. Lin, D. Zan, J. J. Yuan, D. L. Cai, *Cell Biochem. Biophys.* **2011**, *60*, 225.

[70] Z. S. Zhu, C. Xie, Q. Liu, X. Zhen, X. C. Zheng, W. Wu, R. T. Li, Y. Ding, X. Q. Jiang, B. R. Liu, *Biomaterials* **2011**, *32*, 9525.

[71] V. P. Torchilin, *J. Microencapsulation* **1998**, *15*, 1.

[72] D. S. Ling, W. Park, Y. Park, N. Lee, F. Li, C. Song, S. G. Yang, S. H. Choi, K. Na, T. Hyeon, *Angew. Chem. Int. Ed.* **2011**, *50*, 11360.

[73] T. D. Schladt, K. Koll, S. Prufer, H. Bauer, F. Natalio, O. Dumele, R. Raidoo, S. Weber, U. Wolfrum, L. M. Schreiber, M. P. Radsak, H. Schild, W. Tremel, *J. Mater. Chem.* **2012**, *22*, 9253.

[74] Y. Lu, L. Dong, L. C. Zhang, Y. D. Su, S. H. Yu, *Nano Today* **2012**, *7*, 297.